Direct ink writing 3D printing of graphene/Al_2O_3 composite ceramics with gradient mechanics

Jiang Fan[1], Ruihua Guan[1], Kangtai Ou[1], Qiang Fu[1,2], Qingxiao Liu[1], Dian-sen Li[3], Hengyu Zheng[1], Youyi Sun[1*]

1.School of materials science and technology, North University of China, Taiyuan 030051, P.R. China.

2.School of Civil and Environmental Engineering, University of Technology Sydney, Ultimo NSW 2007, Australia.

3.School of Chemistry, Beijing University of Aeronautics and Astronautics, 100191, Beijing, China.

Abstract: A new graphene/Al_2O_3 composite ceramic with tunable mechanics is prepared by direct ink writing (DIW) 3D printing technology. It is found that the bending strength, fracture toughness and hardness all increase with increasing in content of graphene. The bending strength, fracture toughness and hardness of graphene/Al_2O_3 composite ceramic (4.0wt‰) are improved to be 45.0%, 40.6% and 21.9% comparing to Al_2O_3 ceramic, respectively. The result is attributed to good reinforcement of graphene and inhibition of Al_2O_3 phase growth by graphene. Furthermore, the gear wheel with gradient mechanics is also designed and fabricated by the DIW 3D printing technology from various graphene/Al_2O_3 composite gels. It exhibits excellent wear resistance and low generation of heat during rotational friction. The work provides a new method to fabricate graphene based ceramics with gradient structure and mechanics for various applications.

Keywords: Direct ink writing, graphene, Al_2O_3, wear-resistant, gradient ceramics.

Responding author: Fax: 86-351-3922949

E-mail address: syyi@pku.edu.cn (YY Sun)

1.Introduction

Al_2O_3 ceramic has attracted lots of attentions due to high compression strength, hardness, wear resistance, chemical stability, temperature stability and corrosion resistance for wide applications in aerospace, electrical and biomedical[1-2]. Typically, the Al_2O_3 ceramic needs the features of a strong, hard, wear-resistant and toughness for some special applications [1]. However, it is difficult to meet above properties for single Al_2O_3 material. Therefore, it needs to use advanced preparation technology to optimize the combination of various materials, forming a new Al_2O_3 composite ceramic with gradient mechanics[3]. For example, the Al_2O_3/TiC/CaF_2 composite ceramic with gradient mechanic was prepared by powder metallurgical process. The gradient mechanic of Al_2O_3 composite ceramic was obtained by adjusting the mass proportion of TiC and CaF_2, which could overcome the conflict between the tribological and mechanical properties of traditional self-lubricating Al_2O_3 composite[4]. A new Al_7Si_5Cu/Al_2O_3 composite ceramic was prepare by combining dynamic freeze casting with pressure infiltration method. The gradient mechanic of Al_2O_3 composite ceramic was obtained by controlling content of Al_7Si_5Cu and micro-structure of lamellar. The composite ceramic exhibited externally hard, strong, and wear-resistant while was also internally soft and tough[5]. The Ni/Al_2O_3 composite ceramic with a gradient structure was also prepared by combining centrifugal casting with magnetic field. The gradient mechanic of Al_2O_3 composite ceramic was obtained by adjusting distribution of Ni phase under magnetic field. The composite ceramic could overcome the conflict between the tribological and brittle properties of traditional self-lubricating Al_2O_3 composite[6]. The ZrO_2/Al_2O_3 composite ceramic with laminated-gradient structure was prepared by powder metallurgical process. The gradient mechanic of Al_2O_3 composite ceramic was obtained by adjusting content of ZrO_2, which could achieve satisfactory strength and tribology properties[7]. The Al/Al_2O_3 composite ceramic was prepared by the radio frequency magnetron sputtering method, in which the gradient mechanic of Al/Al_2O_3 composite ceramic was obtained by adjusting content of Al. The composite could overcome the conflict between the coating adhesion and mechanical strength[8]. The VC/Cr_3C_2/TiB_2/TiC/Al_2O_3 composite ceramic was prepared by a vacuum hot-press sintering method, in which the gradient mechanic of Al_2O_3 composite ceramic was obtained by adjusting content of VC/Cr_3C_2. The composite could overcome the conflict between the hardness, fracture toughness and flexural strength[9].

The ZrO_2-Y_2O_3/Al_2O_3 composite ceramic was prepared by the multilayer deposition, in which the gradient mechanic of Al_2O_3 composite ceramic was obtained by adjusting content of ZrO_2-Y_2O_3. The composite could overcome the conflict between the hardness, fracture toughness and flexural strength[10]. From above respects, the Al_2O_3 composite ceramic with gradient mechanic had been fabricated by the frequency magnetron sputtering, centrifugal casting, powder metallurgical, electrophoretic deposition or freeze casting. However, these conventional fabricating techniques were only capable of constructing Al_2O_3 composite ceramic with simple shapes and gradient patterns. To produce Al_2O_3 composite ceramic with complex geometries and three-dimensional (3D) compositional gradients, a new technology should be developed.

3D printing technique was a promising method to fabricate Al_2O_3 composite ceramic with complex and 3D geometries, such as binder jetting (BJ), stereolithography appearance (SLA), selective laser sintering (SLS), extrusion freeforming (EFF), direct ink writing (DIW), etc. Among these 3D printing technologies, DIW was the most versatile AM technique for Al_2O_3 composite ceramic due to be suitable for combining more materials with Al_2O_3. For example, a complex Al_2O_3 ceramic part was fabricated by 3D DIW printing method, which exhibited good mechanical properties[11]. A new Al_2O_3/Na_2SiO_3/organic binder ink was developed and prepared for 3D DIW printing to reduce the cost of 3D printing materials[12]. A new Al_2O_3 composite ceramic was fabricated by 3D DIW printing method, in which the sintering temperature was investigated in detail for catalytic application[13]. A $Al(H_2PO_4)/Al_2O_3$ ceramic with ultra-low dimensional shrinkage was also prepared by 3D DIW printing method[14]. These 3D DIW printing Al_2O_3 composite ceramics still showed low mechanical properties. Therefore, a new 3D DIW printing process should be developed to improve the mechanical properties of Al_2O_3 composite ceramics. Furthermore, 3D printing technology was few used to fabricate Al_2O_3 composite ceramic with gradient mechanics.

As well-known, the graphene nanosheet was a promising reinforcement material, which could significantly enhance mechanical and conductive properties of Al_2O_3 ceramic[15-16]. For example, Kawasaki et al reported the preparation and conductive performance of graphene/Al_2O_3 composite ceramic by combining ex-situ strategy with spark plasma sintering method[17]. Sofer et al reported the preparation of graphene/Al_2O_3 composite ceramic with highly electrical conductivity and low heat transfer rate for application in high temperature fuel cell technologies[18]. Jastrze zbska

reported the preparation of RGO/Al_2O_3 composite ceramic, in which the Al_2O_3 nanoparticles were deposited on surface of graphene by a dry sol-gel process[19]. Jiang et al reported the preparation and conductive performance of graphene/Al_2O_3 composite ceramic by ball milling method[20]. Graphene/Al_2O_3 composite ceramic membrane was formed by sequentially depositing layers of graphene and Al_2O_3 for the detection of DNA or DNA protein complexes[21]. From above respects, the graphene nanosheet should be a promising additive for fabricating the Al_2O_3 composite ceramic with gradient mechanics. However, up to now, the graphene/Al_2O_3 composites with gradient structure is still not reported. Furthermore, these graphene/Al_2O_3 composites were mainly based on powders, bulk solids and films. So, it was also high interesting to fabricate the graphene/Al_2O_3 composite ceramic with complex 3D structure by 3D printing technology. Recently, the rGO/Al_2O_3 composite ceramic with complex 3D architecture was prepared by a combination of 3D printing technique and thermal reduction process[15]. The rGO/Al_2O_3 composites were also fabricated by DIW 3D printing technique for application in catalyst field[16]. Although DIW printing graphene/Al_2O_3 composite ceramics have been reported, yet, it is still a high challenge to obtain graphene/Al_2O_3 composite ceramic with low shrinkage and high mechanical performance.

Based on above considerations, a new graphene/Al_2O_3/PVA/CA/TEOA ink material is developed for DIW 3D printing graphene/Al_2O_3 composite ceramic. It can be found that the mechanical properties of graphene/Al_2O_3 composite ceramic are easily tuned by the content of graphene. Furthermore, the graphene/Al_2O_3 composite ceramic with a gradient mechanic is also fabricated by DIW 3D printing technique from graphene/Al_2O_3/PVA/CA/TEOA ink material with various contents of graphene. The work provides a new method to fabricate graphene/ceramic devices with well-established gradient architecture for various applications.

2.Experimental

2.1 Materials

Alumina (Al_2O_3, D_{50}=50μm) was purchased from Germany almatis Co., Ltd. Yttrium stabilized zirconia (3Y-ZrO_2, D_{50}=20nm) was purchased from Shandong Jinan Zhiding welding materials Co., Ltd. Magnesium oxide (MgO, D_{50}=45μm) and polyvinylpyrrolidone (PVP, >99.9%) were purchased from Tianjin Zhiyuan Chemical Reagent Co., Ltd. Polyvinyl alcohol (PVA-1788) and graphite were purchased from

McLean. Triethanolamine (TEOA, >99.9%), citric acid (CA, >99.9%), potassium permanganate ($KMnO_4$, >99.9%), sodium carbonate (Na_2CO_3, >99.9%), phosphoric acid (H_3PO_4, 75%) and concentrated sulfuric acid (H_2SO_4, 99.8%) were purchased from Tianjin Damao chemical reagent factory.

2.2 Preparation of polyvinylpyrrolidone@graphene (PVP@G)

The PVP@G was prepared by a two-steps method as shown in following. Firstly, the expanded graphite (EG) was prepared by bubbling expansion method. 30.0g $KMnO_4$ was added to 180.0mL concentrated sulfuric acid in the ice bath. 30.0g natural graphite was added to above solution under mechanical stirring at room temperature for 1.0h. Then, 30.0g Na_2CO_3 was added to above mixture under mechanical stirring. 420.0mL H_3PO_4 was added into above mixed system under mechanical stirring for 5.0h. Thereafter, the products were washed and filtered, forming EG. Secondly, 10.0g EG and 40.0g PVP were added to 500.0mL NaOH solution (pH=14). The mixture was mechanical agitation for 2.0h at 15000 rpm by using an FA 40 high shear dispersing emulsifier (Fluko). The above dispersion solution was filtered and washed, obtaining PVP@G products. The purified PVP@G was again dispersed in aqueous solution, forming PVP@G dispersion solution (5.0wt%)

2.3 Preparation of 3D printing PVP@G/Al_2O_3 composite gels

10.0g PVA was dissolved in 90.0g deionized water under mechanical stirring at 95.0℃, forming PVA solution with a concentration of 10.0wt%. 5.0g PVA solution (10.0wt%), 1.5g triethanolamine and 3.5g citric acid were mixed under mechanical stirring (500rpm) for 3.0min, forming PVA hydrogel. The PVP@G was added to above PVA hydrogel under mechanical stirring (500rpm) for 2.0min, forming G/PVA hydrogel. The Al_2O_3, 3Y-ZrO_2 and MgO particles were mixed by ball mill for 2.0h. Above mixed particles were further added to 3D printing PVP@G/Al_2O_3 composite gels under mechanical stirring (500rpm). In a comparison, the 3D printing composite gels with various contents of graphene were also prepared as shown in Table 1.

Table 1. Formulation of 3D printing PVP@G/Al_2O_3 composite gels.

PVP@G solution (g)	PVA solution (g)	TEOA (g)	CA (g)	Al_2O_3 (g)	3Y-ZrO_2 (g)	MgO (g)
0.0	5.0	1.5	3.5	21.0	3.0	0.1
1.0	5.0	1.5	3.5	26.0	3.0	0.1

2.0	5.0	1.5	3.5	29.0	3.0	0.1
3.0	5.0	1.5	3.5	32.0	3.0	0.1

2.3 3D printing of graphene/Al_2O_3 composite ceramic

The graphene/Al_2O_3 composite ceramic was fabricated by DIW 3D printing method as shown in Scheme 1A. The 3D printing process was carried out on a DIW printing equipment with a screw extrusion printing head (Scheme 1B) at room temperature[22]. The PVP@G/Al_2O_3 composite gel was added to the printing head and extruded through a nozzle (0.6mm) according to CAD model. The overlap rate in the print setting and the print speed was 100.0% and 10.0mm/min, respectively. The 3D printing composite gel was dried at 40.0℃ for 12.0h. After then, the 3D printing composite ceramic was further debinding at 350.0℃ and 700.0℃ for 2.0h and 2.0h, respectively. Finally, the 3D printing composite ceramic was sintered at 1550.0℃ for 2.0h in a tube furnace under nitrogen atmosphere (Scheme 1A).

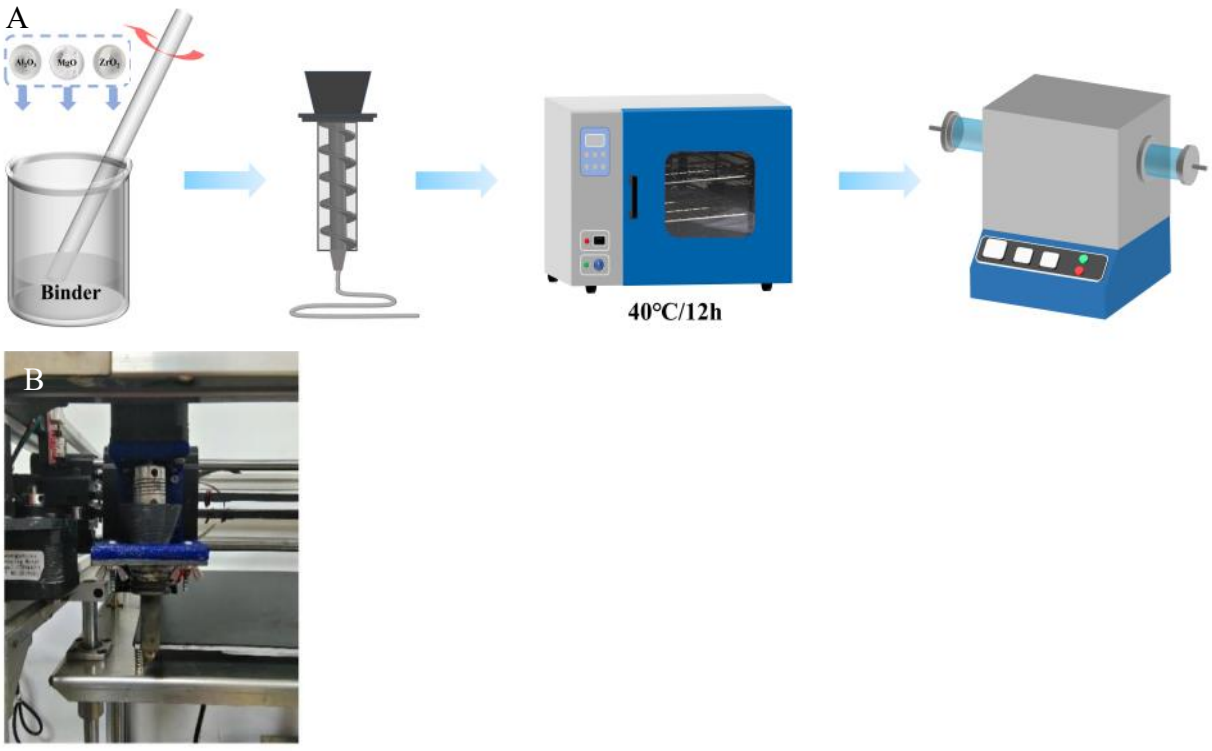

Scheme 1. (A)The Schematic diagram of 3D printing process and (B) Optical photo of 3D printing head.

2.4 Micro-structural characterization

The surface micro-structure of 3D printing composite ceramic was characterized by scanning electron microscopy (SEM, SU-8010) at an accelerating voltage of 5.0kV. The 3D printing samples were soaked in liquid nitrogen and broken into

particles with a size of ca.2.0mm, which acted as testing samples. Average grain size was calculated by analyzing SEM images with the cell counter plugin in ImageJ.

The X-ray diffraction (XRD) of composite ceramic was characterized by Bruker D8 advance with Cu K α radiation at 40.0kV and at an angle of 2θ=5.0~80.0°.

The Fourier transform infrared (FT-IR) spectrum of the gel was tested by Fourier transform infrared spectrometer (thermo Nicolet 360) in the range of 500.0~4000.0cm^{-1}.

The open porosity (*P*, %) and bulk density (ρ, g/cm^3) of composite ceramic were measured by Archimedes drainage method[23].

$$P=\frac{M_3-M_1}{M_3-M_2}\times 100\% \qquad (1)$$

$$\rho=\frac{M_1\times D_L}{M_3-M_2} \qquad (2)$$

Where D_L (g/cm^3) is the density of the water in the test process, M_1 (g) and M_2 (g) are the weight of composite ceramic before and after in water, respectively. M_3 is the weight of the composite ceramic filled with water .

Relative density ρ_{re} was calculated according to following formula (3)

$$\rho_{re}=\frac{\rho}{\rho_{th}} \qquad (3)$$

Where ρ and ρ_{th} are the real and theoretical density of composite ceramic, respectively.

2.5 Mechanical testing

The rheological properties (eg. viscosity and shear-modulus) of printing gel were characterized by rotary rheometer (MCR 302, Anton Paar, Austria). A steady-state mode with a shear rate of 0.01~200.0s^{-1} was used for measuring viscosity. The storage modulus (G′) and loss modulus (G″) were measured in an oscillation free mode with an angular frequency of 10.0rad/s as a function of shear stress from 0 to 100Pa.

The wear resistance of composite ceramic was characterized by Taber wear tester (GT-7012-T) as shown in following. The testing sample was put on the Taber wear tester. The H-22 grinding wheel was used and a load of 500.0g was applied. The testing speed was 60.0rpm/min. The composite ceramic directly acted as wear testing sample. The wear resistance was evaluated by measuring weight loss (*W*, %), which was calculated according to the formula (4). The wear rate (W') was calculated by formula (5).

$$W = \frac{W_o - W_t}{W_o} \times 100\% \quad (4)$$

$$W' = \frac{W}{2\pi R t n \mu P \rho} \quad (5)$$

The W_o *and* W_t are the weight of composite or gear wheel before and after wear testing for 24.0h. ρ (g/cm^3) is the density of the sample, R (m) is the average friction radius , that is the distance between the center of the block sample and the center of the rotation axis, t (min) is the test time , and n (r/min) is the speed, μ is the average friction coefficient of the friction pair, and P (N) is the normal force applied to the sample.

The Vickers hardness of composite ceramic was characterized by Vickers hardness tester (TUkon 2100b). The testing sample was cylindrical shape with a diameter of 30.0mm and a height of 5.0mm. While each sample was held for 10.0s, a load of 294.0N was applied for testing. The fracture surface of testing sample was characterized by the SEM images. The fracture toughness was also calculated according to formula (6)[24].

$$K_{IC} = 0.0134 \left(\frac{E}{H}\right)^{1/2} \frac{P}{C^{3/2}} \quad (6)$$

K_{IC} (MPa·m$^{1/2}$) is the fracture toughness, P (N) is the applied load by the Vickers hardness tester, E (GPa) is the Young's modulus, H (GPa) is the hardness and C (m) is equal to diagonal half-length of Vickers indentation plus crack length (m).

The flexural strength of the composite ceramic was characterized by three-point bending test in an electronic universal testing machine (CMT4304, Suns). The testing sample was rectangular shape (3.0mm×4.0mm×30.0mm). The loading speed was 0.5mm/min and the distance between two points was 20.0mm. The average flexural strength was obtained from three samples.

2.6 Wear resistance of gear wheel based on graphene/Al_2O_3 composite ceramic

The gear wheel with gradient mechanics was fabricated by DIW 3D printing technology from graphene/Al_2O_3 with various contents of graphene. The pattern of gear wheel was generated from the 3D software (CAD) as shown in Scheme 2A. According to the pattern of gear wheel, various graphene/Al_2O_3 ink materials were printed, forming gear wheel with a gradient structure (Scheme 2A). In a comparison, the gear wheel based on pure Al_2O_3 ceramic was also fabricated by similar process.The wear resistance of gear wheels was characterized as shown in Scheme 2B. The two gear wheels rotated at 1500.0rpm for 24.0h. The wear resistance was evaluated by measuring

weight loss according to above formula (4). The surface temperature of various positions in gear wheel was determined by the Thermal imager.

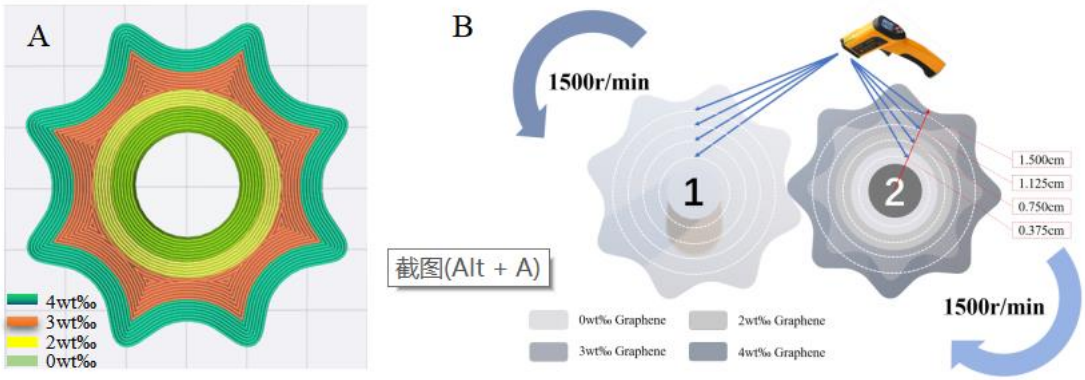

Scheme 2. (A) Schematic diagram of gear wheel with gradient mechanic, (B) Schematic diagram of wear testing for gear wheel.

3.Results and discussion

In this study, a novel graphene/Al_2O_3 composite gel with shear-thinning effect acts as ink material for DIW 3D printing (Fig.1A). The graphene/Al_2O_3 composite gel was facile preparation by mixing process. It was composed of PVA, TEOA, CA, Al_2O_3, 3Y-ZrO_2, PVP@G and MgO. The hydrogen bond was formed between -OH of PVA and -COO^- of CA, producing the cross-linking structure. The cross-linking structure was key role for formation of PVA/CA gel (Fig.1B). TEOA was also introduced to improve the strength, mechanical stability and moisture retention of PVA/CA gel, avoiding collapse of 3D printing sample and the clogging of the nozzle. Moreover, the PVA/CA gel also showed good universality, in which other materials (eg. Al_2O_3, 3Y-ZrO_2, PVP@G and MgO) could be added to the PVA/CA gel, forming various 3D printing ink materials. In addition, these inorganic particles were also well dispersed in PVA/CA gel due to the amphipathic character of TEOA and gel state, which was key role for DIW 3D printing technology. Here, ZrO_2 and MgO acted as inclusion and sintering aid to restrain the phase growth and reduce sintering temperature of Al_2O_3 ceramic, respectively[14]. The formation of PVA/CA/TEOA gel was confirmed by the FT-IR spectrum as shown in Fig.1C. A strong peak at 3320.0cm^{-1} and weak peak at 2849.0cm^{-1} were clearly observed, which were assigned to the -OH and C-H stretching vibration of PVA, respectively. The absorption peak at 1713.0cm^{-1} was assigned to C-O-C asymmetric stretching vibration of CA. A new peak at 1218cm^{-1} was also observed, which was assigned to strong hydrogen bond between -OH of PVA and -COO^- of CA. Furthermore, the hydrogen

bond was easily destroyed during shear and re-establish after removal of the shear force. These characters leaded to a good shear-thinning effect, which was also key role for DIW 3D printability for present gels.

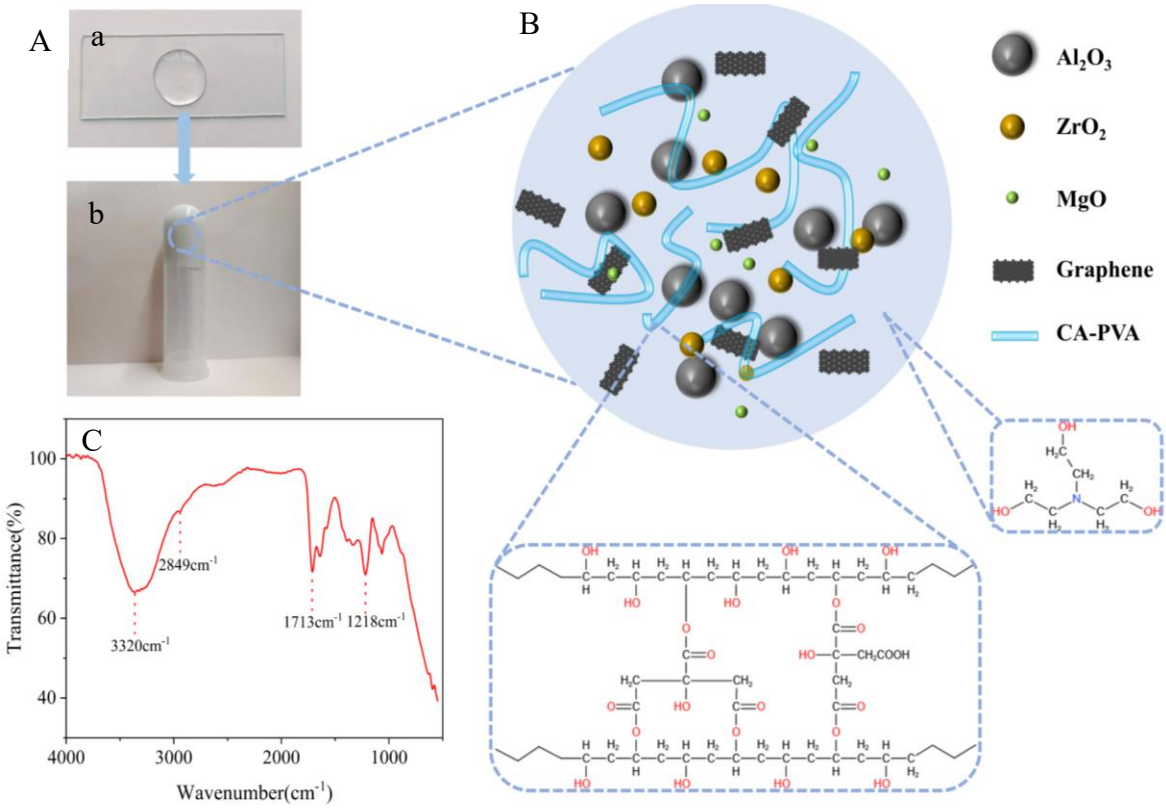

Fig.1. (A) Optical photo of (a) PVA/CA/TEOA gel and (b) graphene/Al_2O_3 composite gel, (B) The Schematic diagram of micro-structure of 3D printing graphene/Al_2O_3 composite gel, (C) FT-IR spectrum of PVA/CA/TEOA gel.

The DIW 3D printability of graphene/Al_2O_3 composite gel was evaluated by rheological behavior as shown in Fig.2. Fig.2A shows the viscosity of graphene/Al_2O_3 composite gel as a function of shear rate. All graphene/Al_2O_3 composite gels exhibited a similar viscosity (η) of ~10^5mPa·s at low shear rate of ~0.1s^{-1}. When the shear rate increased from 0.1s^{-1} to 200s^{-1}, the η of all graphene/Al_2O_3 composite gels dramatically decreased from 10^5 to 10^3mPa·s. The result confirmed the good shear-thinning effect of present graphene/Al_2O_3 composite gel. In a comparison, the graphene/Al_2O_3 composite gels with higher content of graphene exhibited better shear-thinning effect. The result was attributed to the formation of hydrogen bonding between graphene and PVA. (inset of Fig.2A). Fig.2B shows the G′ and G″ of all graphene/Al_2O_3 composite gels as a function of shear stress. It was found that the G′ was significantly higher than

the G″, indicating a gel state. The shear yield stress (τ_y) of graphene/Al_2O_3 composite gels was about 35.1Pa, 15.4 Pa, 9.8Pa and 7.7Pa for various graphene contents of 0.0wt‰, 2.0wt‰, 3.0wt‰ and 4.0wt‰, respectively. The large shear yield stress provided high shape fidelity of DIW 3D printing graphene/Al_2O_3 composite gel. These graphene/Al_2O_3 composite gels were ideally suited for DIW 3DP process.

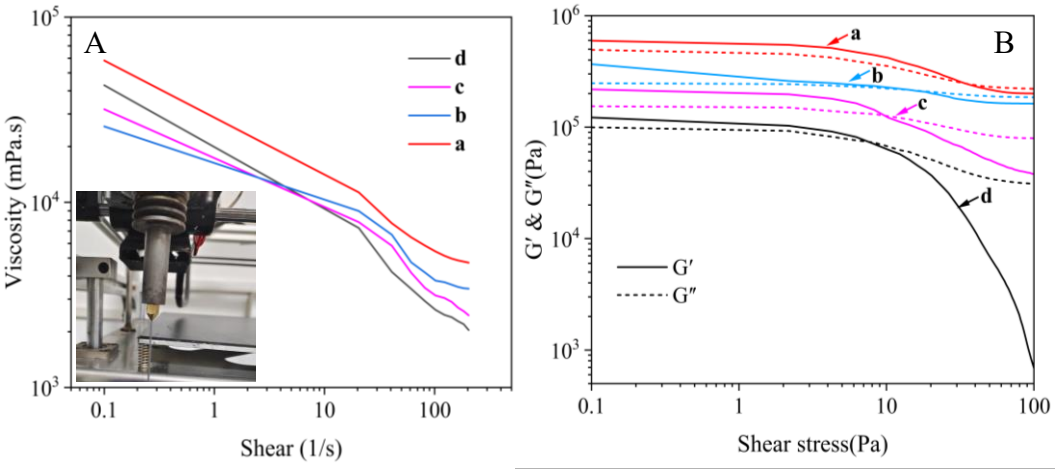

Fig.2. (A) viscosity *vs* shear rate curves and (B) modulus *vs* shear stress curves of graphene/Al_2O_3 composite gels with various graphene contents of (a)0.0wt‰, (b)2.0wt‰, (c)3.0wt‰ and (d)4.0wt‰. The inset of A is optical photo of graphene/Al_2O_3 composite gel in DIW printing process.

To further demonstrate excellent printability of present graphene/Al_2O_3 composite gels, cylinder, box and butterfly were fabricated by DIW 3D printing technology from the graphene/Al_2O_3 composite gel as shown in Fig.3A. The shape and size of 3D printing graphene/Al_2O_3 composite gels were almost same with the CAD model. It exhibited good structural fidelity and high resolution of graphene/Al_2O_3 composite gel, further demonstrating excellent printability. Furthermore, the shape and size of 3D printing graphene/Al_2O_3 composite gels were almost identical before and after thermal drying. These results were attributed to the high solid content (>80.0wt%) of graphene/Al_2O_3 composite gels, reducing the shrinkage or deformation. As well-known, α-Al_2O_3 with lattice structure was difficult to be fabricated by the conventional die and processing method due to high hardness and brittleness. It further confirmed that the 3D printing technology was a promising method to fabricate 3D α-Al_2O_3 complex structure. Fig.3B shows the TG/DTG curves of graphene/Al_2O_3 composite gel. It clearly showed two zones. The first zone exhibited a mass loss of ca.10.0% at less temperature than 220.0℃, which was attributed to the evaporation of water. The second

zone showed a mass loss of ca.7.8%, which was assigned to degradation of the organic composition (eg. PVA, TEOA, CA) in the range of 250~700.0℃. The result further confirmed the high solid content (>80.0wt%) of present graphene/Al_2O_3 composite gel.

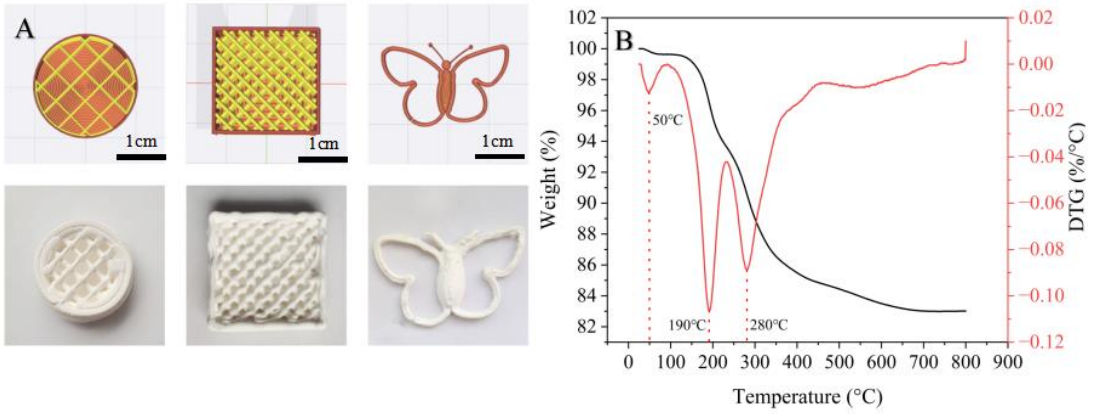

Fig.3. (A) CAD models (up) and optical photos (down) of 3D printing graphene/Al_2O_3 composite gels. (B) TG/DTG curves of graphene/Al_2O_3 composite gel (4.0wt‰).

Fig.4A shows the XRD patterns of 3D printing Al_2O_3 and graphene/Al_2O_3 composite ceramic. Some strong diffraction peaks at 2θ=25.8°, 35.5°, 38.1°, 43.6°, 52.8°, 57.7°, 61.5°, 66.8°, 68.5° and 77.1° were clearly observed, which were assigned to (012), (104), (110), (113), (024), (116), (211), (214), (300) and (208) planes of α-Al_2O_3 (JCPDS card No. 78-2426)[22]. In addition, some new diffraction peaks at 2θ=30.3°, 50.6°, 60.1°, 62.9° were also observed, corresponding to (101), (200), (211), and (202) planes of ZrO_2 (JCPDS card No. 88-1007)[10]. The diffraction peak of graphene was not found due to ultra-low doped content and amorphous of graphene. The Raman spectra of 3D printing Al_2O_3 and graphene/Al_2O_3 composite ceramics were further characterized and compared as shown in Fig.4B. For 3D printing Al_2O_3 ceramic, there was no absorption in the range of 1000.0~2500.0cm^{-1} (Fig.4B-a). In contrast, it clearly showed two absorption peaks at 1355.0cm^{-1} and 1587.0cm^{-1} (Fig.4B-b), which were assigned to D and G bands of graphene[25]. In addition, the G peak of graphene in present composite ceramic was red shift from 1576.0cm^{-1} to 1587.0cm^{-1} comparing to traditional reduced oxide graphene. It indicated more sp^2 orbitals and higher reducing degree for present graphene, resulting from the high sintering temperature[15]. These results indicated the formation of graphene/Al_2O_3 composite ceramic by DIW 3D printing technology.

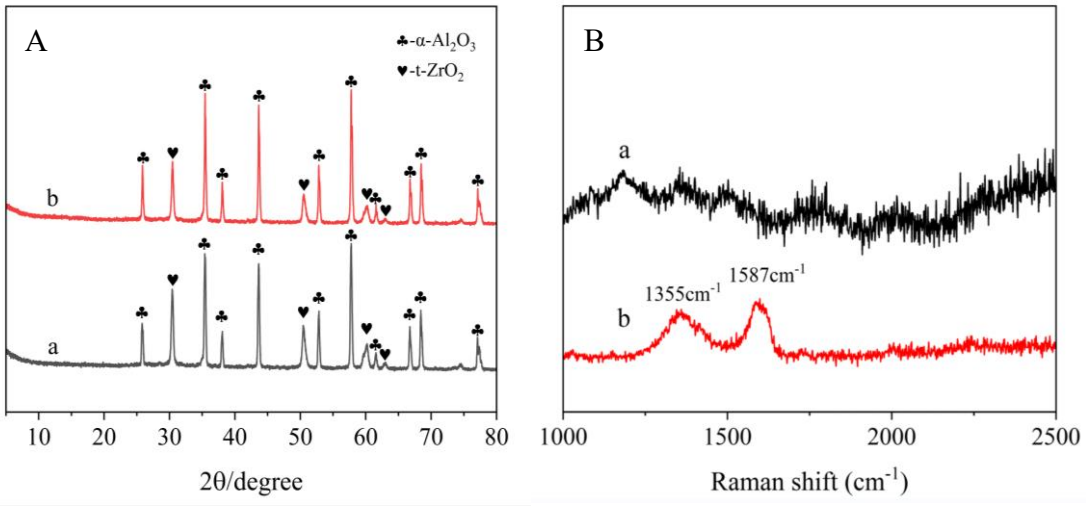

Fig.4. (A) XRD and (B) Raman spectra of 3D printing (a) Al_2O_3 and (b) graphene/Al_2O_3 composite ceramic (4.0wt‰).

The micro-structure of 3D printing graphene/Al_2O_3 composite ceramics was further characterized by the SEM images as shown in Fig.5. All graphene/Al_2O_3 composite ceramics obviously displayed relatively high compact structure and less large porous structures comparing to previous DIW 3D printing ceramics[15-16, 26]. The different result was attributed to high solid content of inorganic particles and thermal drying of present DIW 3D printing ceramics. However, lots of μm-scale pores were clearly observed, resulting from water evaporation of hydrogel and degradation of organic composition. The effect of graphene on size distribution of Al_2O_3 phases in graphene/Al_2O_3 composite ceramics was also determined by SEM images and the result was concluded in Fig.5E. The average value of Al_2O_3 phases was about 3.7um, 2.3um, 2.1um, and 1.8um for graphene/Al_2O_3 composite ceramics with 0wt‰, 2.0wt‰, 3.0wt‰ and 4.0wt‰, respectively. The result confirmed that the size of Al_2O_3 phases in graphene/Al_2O_3 composite ceramics decreased with increasing in content of graphene. The result was attributed to good pinning effect of graphene nanosheets[25]. When graphene/Al_2O_3 composite ceramic was high-temperature sintering, the Al_2O_3 phase was general mobility, forming larger Al_2O_3 phase[27]. Here, mobility of the Al_2O_3 phase was pinned by graphene nanosheets, reducing size of Al_2O_3 phase. Furthermore, compared with other materials (eg. WC, ZrO_2), the graphene was more efficient to inhibit mobility of Al_2O_3 phase due to ultra-high strength and high-temperature stability. The cross-section EDS mapping images of graphene/Al_2O_3 composite ceramics were further characterized and compared as shown in Fig.5F. The C element was clearly

observed for all composite ceramics, which was assigned to graphene. In addition, it was also found that the C element was uniform distribution on EDS mapping images. These results further confirmed the formation of graphene/Al_2O_3 composite ceramics with uniform dispersion. The EDS spectrum of 3D printing graphene/Al_2O_3 composite ceramic (4.0wt‰) was also characterized as shown in Fig.5G. Five peaks were clearly observed, which were assigned to C, O, Mg, Al and Zr element. Here, the Mg, Al and Zr element resulted from MgO, Al_2O_3 and ZrO_2, respectively. The C element was assigned to graphene and carbonization of organic materials (eg. PVP, PVA, CA and so on). The content of C was about 0.6% according to content of C (0.6wt%), O(45.5wt%), Mg (0.1wt%), Al (47.6wt%) and Zr (6.2wt%) element, which was higher than content (4.0wt‰) of graphene. The result was attributed to carbonization of organic materials. These results further confirmed the formation of graphene/Al_2O_3 composite ceramics.

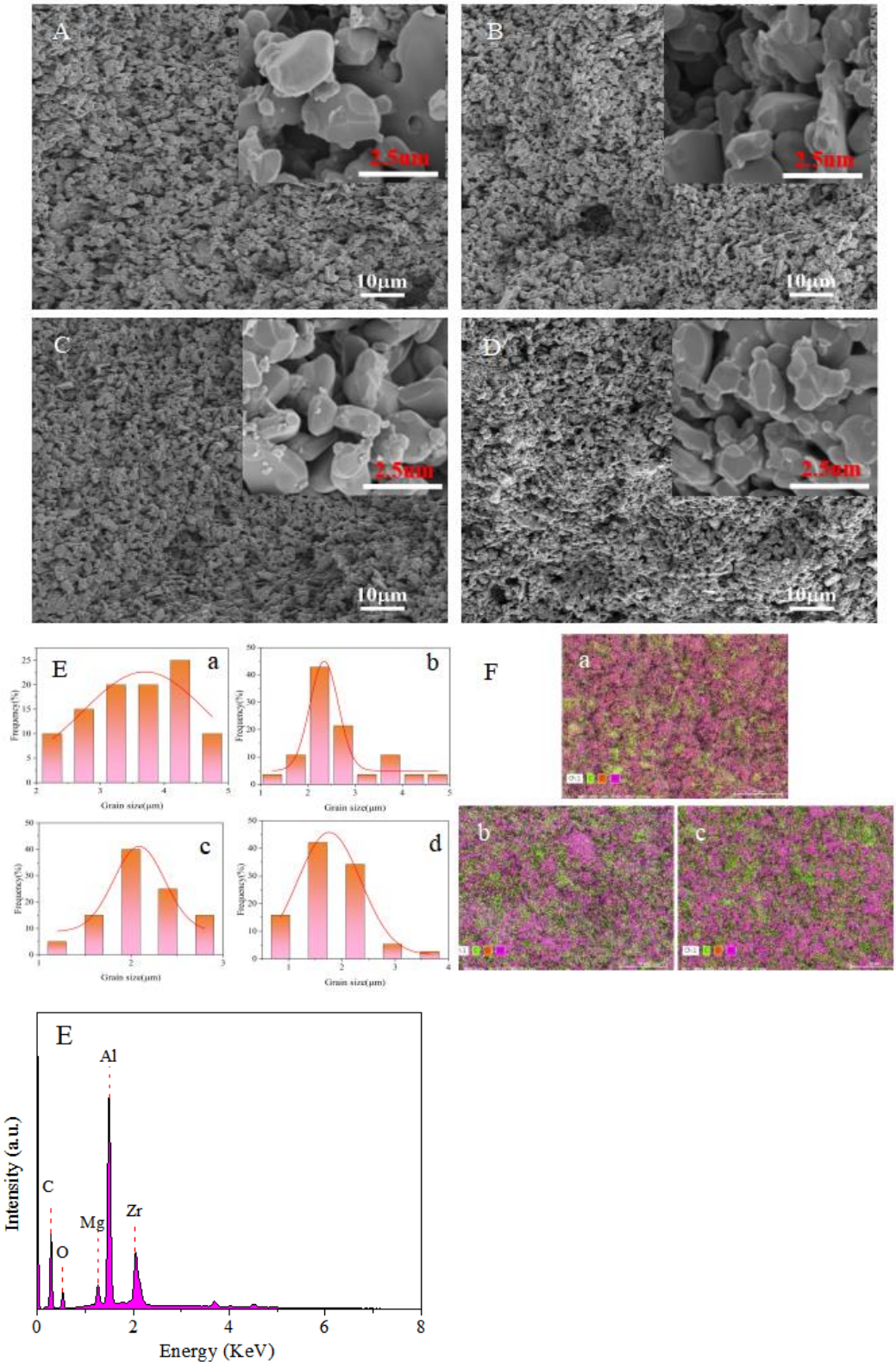

Fig.5. SEM images of 3D printing graphene/Al_2O_3 composite ceramics with different contents of graphene, (A)0wt‰, (B)2.0wt‰, (C)3.0wt‰ and (D)4.0wt‰. (E) size distribution of Al_2O_3 phases in 3D printing graphene/Al_2O_3 composite ceramics with different contents of graphene, (a)0wt‰, (b)2.0wt‰, (c)3.0wt‰ and (d)4.0wt‰. (F)

EDS mapping images of 3D printing graphene/Al_2O_3 composite ceramics with various contents of graphene, (a)2.0wt‰, (b)3.0wt‰ and (c)4.0wt‰, the green, orange and pink part represents C, O and Al element, respectively. (E) EDS spectrum of 3D printing graphene/Al_2O_3 composite ceramic (4.0wt‰), The insets of (A-D) correspond its magnification images.

The open porosity of 3D printing graphene/Al_2O_3 composite ceramics was characterized as a function of graphene content as shown in Fig.6A. The porosity of 3D printing graphene/Al_2O_3 composite ceramics decreased with increasing in content of graphene. The decrease in open porosity was mainly attributed to that the graphene could effectively inhibit mobility of Al_2O_3 phase, reducing the number of micropores[28]. Fig.6B shows the bulk density of 3D printing graphene/Al_2O_3 composite ceramics as a function of graphene content. As expected, the bulk density of 3D printing graphene/Al_2O_3 composite ceramics obviously increased with increasing in content of graphene. The result was attributed to less pores (or smaller porosity) for 3D printing graphene/Al_2O_3 composite ceramics with higher content of graphene[29]. In addition, the relative density of 3D printing graphene/Al_2O_3 composite ceramics was also characterized as shown in Fig.6C. The relative density also increased with increasing in content of graphene. It was found that the 3D printing graphene/Al_2O_3 composite ceramic (4.0wt‰) exhibited large relative density of ca. 96.2%. This result further confirmed the low porosity of present 3D printing graphene/Al_2O_3 composite ceramics. The volume shrinkage of 3D printing graphene/Al_2O_3 composite ceramics after debinding and sintering process was also characterized as a function of graphene content as shown in Fig.6D. As expected, the volume shrinkage of 3D printing graphene/Al_2O_3 composite ceramics decreased with increasing in content of graphene during the debinding and sintering process. The volume shrinkage of 3D printing graphene/Al_2O_3 composite ceramics was attributed to removal of water and organic component in the debinding process. In a comparison, the volume shrinkage of 3D printing graphene/Al_2O_3 composite ceramics was attributed to fusion and bonding of Al_2O_3 particles in the sintering process, indicating a small volume shrinkage (ca.2%). When the content of graphene was about 4.0wt‰, the volume shrinkage of 3D printing graphene/Al_2O_3 composite ceramics was about 5.7%. The slight volume shrinkage was due to high solid content and addition of graphene of graphene/Al_2O_3 composite gel.

The low volume shrinkage of DIW 3D printing objects was also key role for practical application.

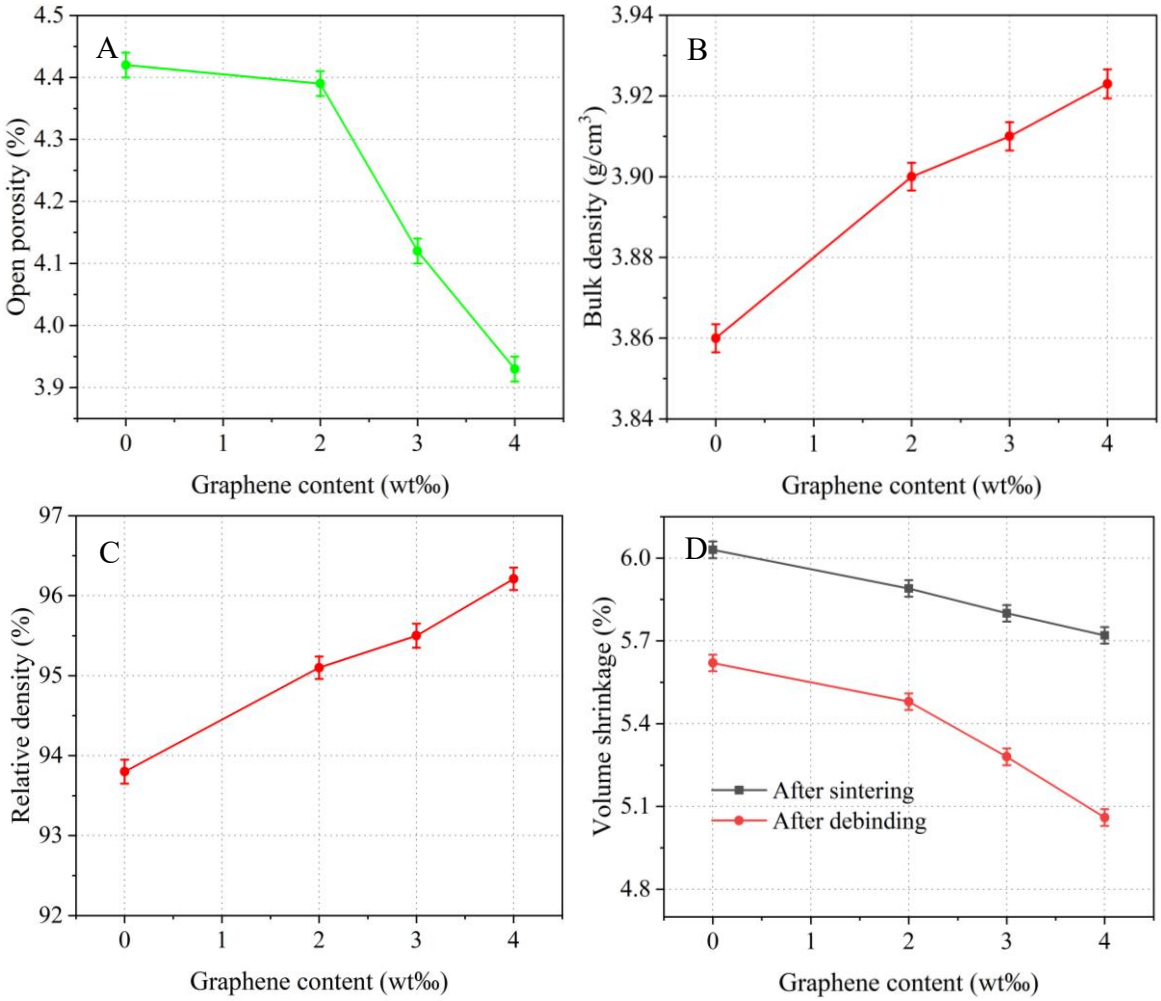

Fig.6. (A) Open porosity, (B) Bulk density, (C) Relative density and (D) Volume shrinkage of 3D printing graphene/Al_2O_3 composite ceramics as a function of graphene content.

Fig.7A shows the bending strength of 3D printing graphene/Al_2O_3 composite ceramics as a function of graphene content. The bending strength of 3D printing graphene/Al_2O_3 composite ceramics obviously increased with increasing in content of graphene. The bending strength of 3D printed graphene/Al_2O_3 composite ceramic (4.0wt‰) was improved to be 45.0% comparing to the 3D printing Al_2O_3 ceramics. Furthermore, present 3D printing graphene/Al_2O_3 composite ceramics exhibited largest bending strength (320.1MPa) comparing to previous DIW 3D printing Al_2O_3 ceramics (Fig.7B)[14, 30]. It also showed larger bending strength comparing to most of other Al_2O_3 ceramics prepared by other 3D printing technology, such as Stereo lithography appearance (SLA), Selective laser melting (SLM), Inkjet printing (IJP) and so on[31-

36]. Fig.7C shows the Vickers hardness of 3D printing graphene/Al_2O_3 composite ceramics as a function of graphene content. It was seen that the graphene could also effectively enhance Vickers hardness. The hardness (150HV) of 3D printing graphene/Al_2O_3 composite ceramic (4.0wt‰) was improved to be 21.9% comparing to that (123HV) of 3D printing Al_2O_3 ceramics. The enhanced bending strength and hardness were attributed to following several reasons. Firstly, the graphene was a good reinforcing materials due to excellent mechanical properties. Secondly, the graphene exhibited good pinning effect and prevented the growth of Al_2O_3 phase, improving mechanical performance[37]. Thirdly, it showed higher compact and smaller porosity by addition of graphene, effectively improving mechanical performance. These results confirmed that the mechanical properties of 3D printing graphene/Al_2O_3 composite ceramics were easily adjusted by the content of graphene. The wear resistance of 3D printing graphene/Al_2O_3 composite ceramics was also characterized and compared as a function of graphene content as shown in Fig.7D. As expected, the weight rate of 3D printing graphene/Al_2O_3 composite ceramics obviously decreased with increasing in content of graphene. It indicated that the 3D printing graphene/Al_2O_3 composite ceramics exhibited better wear resistance at higher content of graphene[37]. The result was due to larger hardness at higher content of graphene for 3D printing graphene/Al_2O_3 composite ceramics.

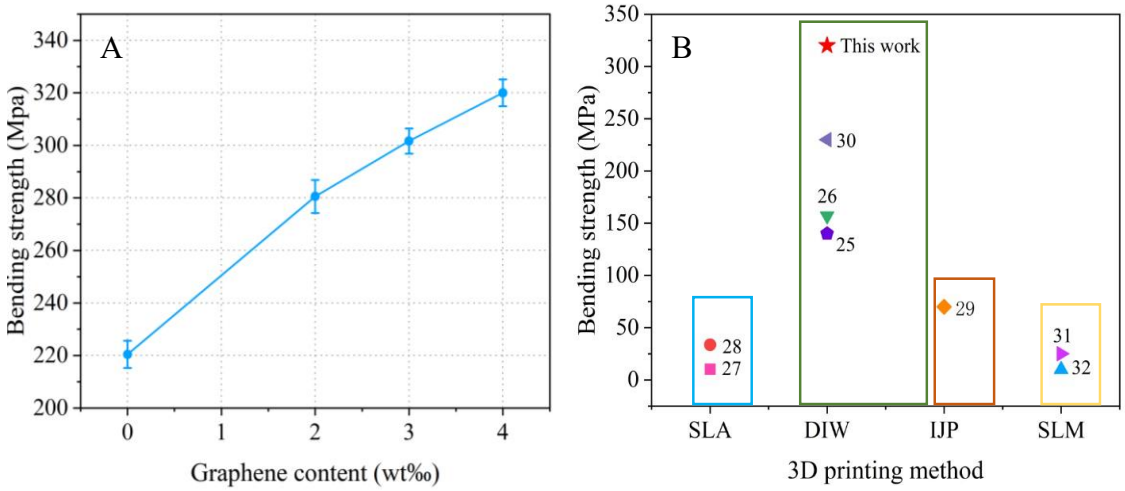

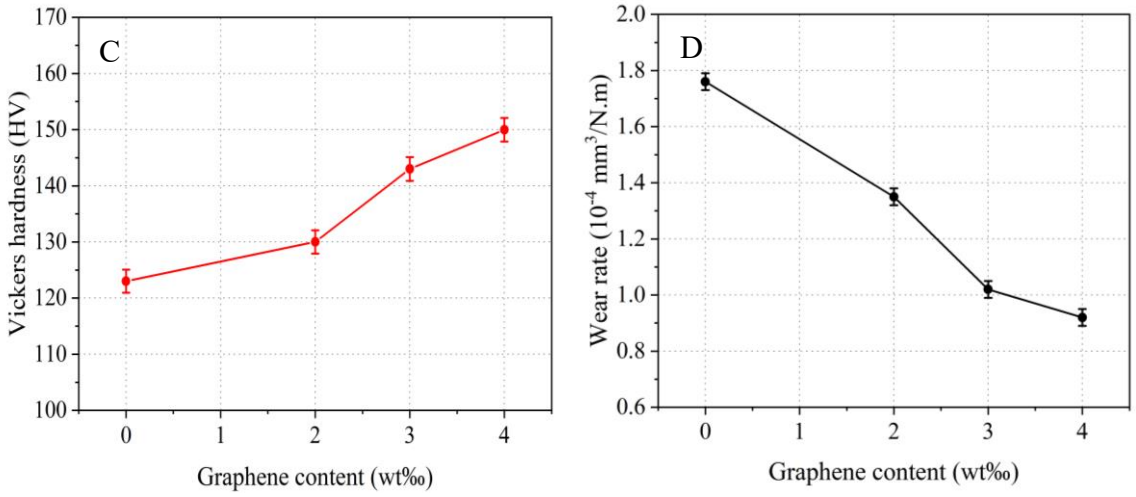

Fig.7. (A) Bending strength of 3D printing graphene/Al_2O_3 composite ceramics with various contents of graphene, (B) Comparison in bending strength of present 3D printing graphene/Al_2O_3 composite ceramics and previous 3D printing Al_2O_3 ceramic, (C) Vickers hardness and (D) Wear rate of 3D printing graphene/Al_2O_3 composite ceramics with various contents of graphene.

Fig.8A shows the fracture toughness of 3D printing graphene/Al_2O_3 composite ceramics with various contents of graphene. The fracture toughness of 3D printing graphene/Al_2O_3 composite ceramics also increased with increasing in content of graphene. When the content of graphene was improved from 0 to 4.0wt‰, the fracture toughness of 3D printing graphene/Al_2O_3 composite ceramics was improved from 3.2MPa·$m^{1/2}$ to 4.5MPa·$m^{1/2}$. The fracture surface of graphene/Al_2O_3 composite ceramics with various contents of graphene was further investigated by SEM images (sFig.1). The fracture surface of graphene/Al_2O_3 composite ceramics was obtained by indentation fracture toughness testing (Fig.8B). It clearly showed more compact structure for graphene/Al_2O_3 composite ceramics with higher content of graphene. As well-known, the compact structure was benefit to improve fracture toughness of ceramics[36-37]. Fig.8C shows the magnification images of graphene/Al_2O_3 composite ceramic (4.0wt‰) with indentation fracture. The smooth fracture surface and cracks were clearly observed for the graphene/Al_2O_3 composite ceramic. The result indicated the brittle fracture characteristics of 3D printing graphene/Al_2O_3 composite ceramics. In addition, it was seen that graphene nanosheets were distributed on the junction of Al_2O_3 phase. When a crack met with graphene nanosheets, it effectively prevented the propagation of crack. It could also change direction of propagation of crack in plane,

leading to an increase of crack propagation path. Generally, the larger crack propagation path exhibited larger fracture toughness [37].

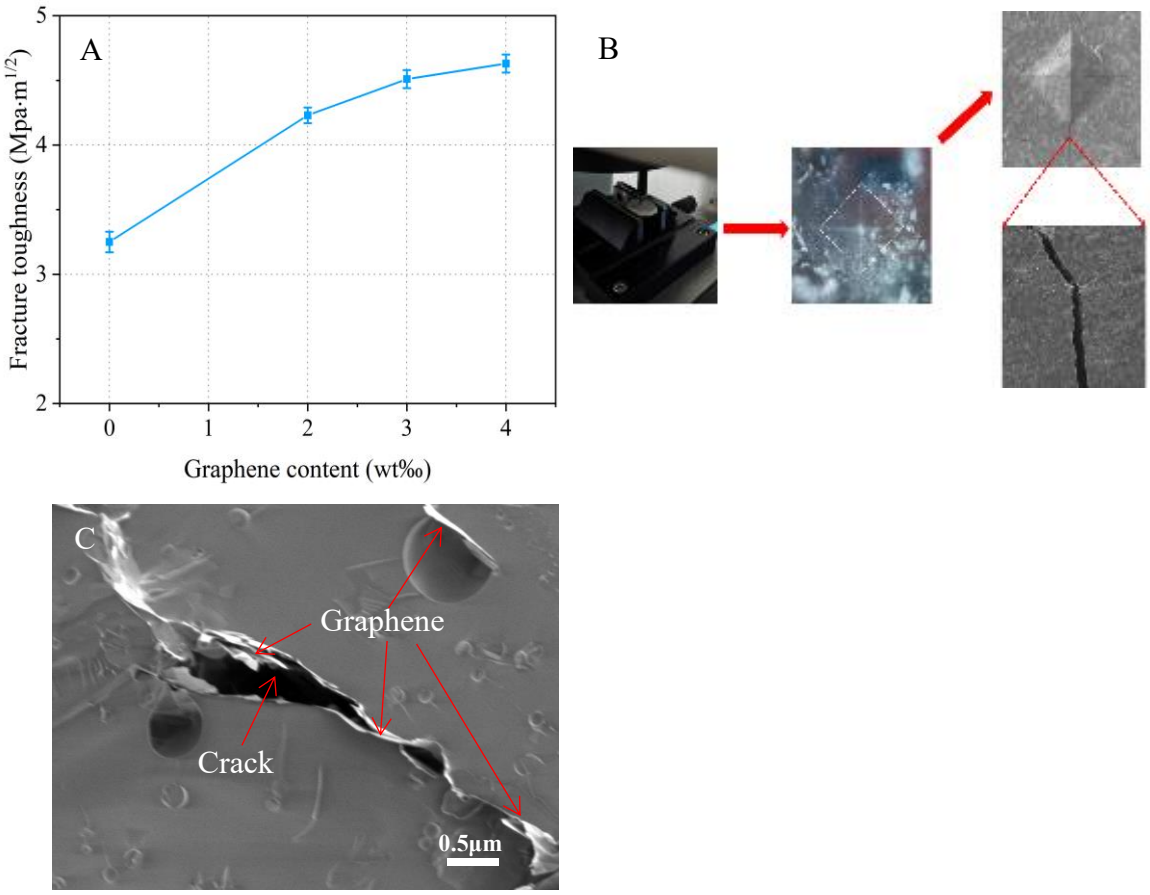

Fig.8. (A) Fracture toughness of 3D printing graphene/Al_2O_3 composite ceramics with various contents of graphene. (B) The Schematic diagram of fracture toughness for 3D printing graphene/Al_2O_3 composite ceramic, (C) Cross-section SEM images of graphene/Al_2O_3 composite ceramics with 4.0wt‰ graphene.

A new gear wheel with gradient structure was designed and fabricated by DIW 3D printing method from graphene/Al_2O_3 composite gels with various contents of graphene as shown in Fig.9A-a. The gradient content of graphene in the 3D printing gear wheel resulted in a gradient in the mechanical behaviour. The mechanical properties (eg. fracture toughness and Vickers hardness) gradually increased along the position from center to outward of the gear wheel (in sFig.2). The wear resistance of gear wheel based on Al_2O_3 and graphene/Al_2O_3 composite was characterized and compared as shown in Fig.9B. The two gear wheels rubbed against each other at 1500.0r/min for 24.0h (in Scheme 2B). The wear rate of 3D printing gear wheel with gradient mechanics was about $0.8\times10^{-4}m^3/N\cdot m$, while it was about $1.2\times10^{-4}m^3/N\cdot m$ for the 3D printing gear wheel based on single Al_2O_3. This indicated that the graphene could effectively improve

wear resistance of gear wheel. The temperature of two 3D printing gear wheels was also characterized and compared by Thermal imager (Fig.9A-b) and the result was concluded in Fig.9C. The temperature of two gear wheels both slightly decreased along the direction from outward to the central region (Fig.9A-b). The result was attributed to the generation of heat by friction from contact surface of two gear wheels. In a comparison, the temperature of gear wheel based on graphene/Al_2O_3 composite was lower comparing to single Al_2O_3. The result was attributed to high thermal conductivity and good thermal radiation properties of graphene, enhancing the heat dissipation. These results indicated that the gear wheel with gradient mechanics exhibited good wear resistance and thermal stability.

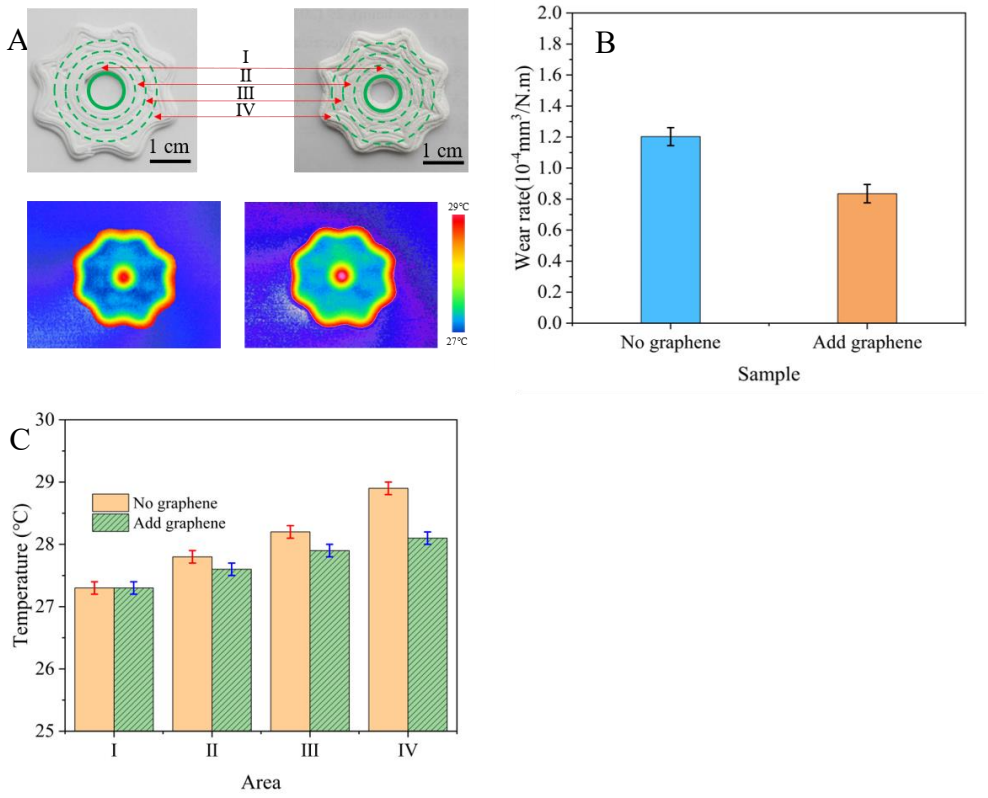

Fig.9. (A) (a) The optical photo and (b) Thermal infrared image of gear wheel based on single Al_2O_3 (Left) and graphene/Al_2O_3 gradient composites (Right). The I, II, III and IV zone of gear wheel with gradient mechanics represent graphene/Al_2O_3 composite with 0wt‰, 2.0wt‰, 3.0wt‰ and 4.0wt‰ graphene, respectively. (B) Wear rate in rotation and (C) Temperature plots in various positions of 3D printing gear wheel under gear friction testing.

4.Conclusions

In summary, a new DIW 3D printing process was developed to facilely fabricate graphene/Al_2O_3 composite ceramics with tunable mechanical proprieties. The bending strength, fracture toughness and hardness were further effectively improved by addition of graphene, even at low content of graphene. Furthermore, the graphene/Al_2O_3 composite ceramics with tunable mechanical proprieties was applied in gear wheel with gradient mechanics. It exhibited excellent wear resistance and thermal stability due to low generation of heat by friction. The work opens up a new method to fabricate graphene based ceramics with gradient structure for various applications.

Acknowledgments

The authors are grateful for the support of the National Natural Science Foundation of China under grants (U1810114), Shanxi Provincial Natural Science Foundation of China (202104021301059, YDZJSX2021A026).

Conflict of interest

The authors declared that they have no conflicts of interest to this work.

References

[1] L. D.M.Barbara, M.P. Ginebra, *J. Eur. Ceram. Soc.* **2021**, *41*, 18.

[2] Z. Chen, Z. Li, J. Li, *J. Eur. Ceram. Soc.* **2019**, *39*, 661.

[3] E. M. M Ewais, D. H. A Besisa, Z. I Zaki, *J. Eur. Ceram. Soc.* **2012**, *32*, 1561.

[4] G. Wu, C. Xu, G. Xiao, *Ceram. Int.* **2018**, *44*, 5550.

[5] L. K Yang, P. Shen, R. F Guo, *Scr. Mater*. **2019**, *167*, 101.

[6] J. Zygmuntowicz, M. Wachowski, A. Miazga, *Composites, Part B*. **2019**, *156*, 113.

[7] Y. E Qi, Y. S Zhang, Y. Fang, *Composites, Part B*. **2013**, *47*, 145.

[8] B. Song, P. Wu, S. Chen, *Surf. Interface Anal*. **2012**, *44*, 466.

[9] F. Gong, J. Zhao, G. Liu, *Ceram. Int.* **2021**, *47*, 20341.

[10] C. Dos Santos, C. M. F. A Cossu, M. F. R. P Alves, *Int. J. Refract. Met. Hard Mater.* **2018**, *75*, 147.

[11] L. Yang, X. Zeng, A. Ditta, *J. Adv. Ceram*. **2020**, *9*, 312.

[12] M. Kotobuki, *Phys. Status Solidi B*. **2021**, *259*, 2100520.

[13] F. Álvarez, A. Cifuentes, I. Serrano, *J. Eur. Ceram. Soc*. **2022**, *42*, 2921.

[14] X. Xu, J. Zhang, P. Jiang, *Ceram. Int.* **2022**, *48*, 864.

[15] C. R Tubío, A. Rama, M. Gómez, *Ceram. Int.* **2018**, *44*, 5760.

[16] J. Azuaje, A. Rama, A. Mallo-Abreu, *J. Eur. Ceram. Soc.* **2021**, *41*, 1399.

[17] Y. Fan, W. Jiang, A. Kawasaki, *Adv. Funct. Mater.* **2012**, *22*, 3882.

[18] O. Jankovský, P. Šimek, D. Sedmidubský, *RSC Adv.* **2013**, *4*, 7418.

[19] A. Maria Jastrzębska, A. Roman Olszyna, J. Jureczko, *Int. J. Appl. Ceram. Technol.* **2015**, *12*, 522.

[20] Y. Fan, L. Wang, J. Li, *Carbon*. **2010**, *48*, 1743.

[21] B. M Venkatesan, D. Estrada, S. Banerjee, *Acs Nano*. **2012**, *6*, 441.

[22] G.Y Yang, Y. Y Sun, L. M Qing, *Compos. Sci. Technol.* **2021**, *215*, 109013.

[23] A. C. H Tsang, J. Zhang, K. N Hui, *Adv. Mater. Technol.* **2022**, *20*, 2101358.

[24] H. Xie, X. Yang, P. Liu, *J. Eur. Ceram. Soc.* **2021**, *41*, 6634.

[25] S. Grigoriev, A. Smirnov, N. W. S Pinargote, *Materials (Basel)*. **2022**, *15*, 2419.

[26] V. R Akhil Raj, K. Hadagalli, P. Jana, *J. Mater. Eng. Perform.* **2021**, *30*, 1234.

[27] Y. Fan, M. Estili, G. Igarashi, *J. Eur. Ceram. Soc.* **2014**, *34*, 443.

[28] A. Arab, Z. D. I Sktani, Q. Zhou, *Materials (Basel)*. **2019**, *12*, 2440.

[29] Q. L Li, X. L An, J. J Liang, *J. Mater. Sci. Technol.* **2022**, *104*, 19.

[30] L. Rueschhoff, W. Costakis, M. Michie, *Int. J. Appl. Ceram. Technol.* **2016**, *13*, 821.

[31] H. Li, Y. S Liu, Y. S Liu, *Mater. Lett.* **2021**, *285*, 129096.

[32] H. Li, Y. S Liu, Y. S Liu, *J. Eur. Ceram. Soc.* **2020**, *40*, 4825.

[33] D. Yao, C. M Gomes, Y. P Zeng, *Mater. Lett.* **2015**, *147*, 116.

[34] E. Feilden, E. G-T Blanca, F. Giuliani, *J. Eur. Ceram. Soc.* **2016**, *36*, 2525.

[35] K. Florio, S. Pfeiffer, M. Makowska, *Adv. Eng. Mater.* **2019**, *21*, 1801352.

[36] M. X Gan, C. H Wong, *Ceram. Int.* **2018**, *44*, 19008.

[37] K. Jiang, J. Li, J. Liu, *Adv. Eng. Mater.* **2015**, *17*, 716.